A peer-reviewed version of this preprint was published in PeerJ on 1 July 2014.

Automated Analysis of Invadopodia Dynamics in Live Cells

Matthew E. Berginski[1#], Sarah J. Creed[2#], Shelly Cochran[1], David W. Roadcap[2], James E. Bear[2,3,4,*] and Shawn M. Gomez[1,5,6,*]

1. UNC/NCSU Joint Department of Biomedical Engineering, University of North Carolina at Chapel Hill, Chapel Hill, NC
2. Department of Cell Biology and Physiology, University of North Carolina at Chapel Hill, Chapel Hill, NC
3. Lineberger Comprehensive Cancer Center, University of North Carolina at Chapel Hill, Chapel Hill, NC
4. Howard Hughes Medical Institute, Chevy Chase, MD
5. Department of Computer Science, University of North Carolina at Chapel Hill, Chapel Hill, NC
6. Department of Pharmacology, University of North Carolina at Chapel Hill, Chapel Hill, NC

Current Addresses:

MEB: Department of Biomedical Engineering, Duke University. 101 Science Drive, Durham NC

SJC: Monash Institute of Pharmaceutical Sciences, Monash University, Parkville VIC Australia

* Address Correspondence To:

Shawn M. Gomez. Tel: +1 919 966 4959. Email: smgomez@unc.edu

or

James E. Bear. Tel: +1 919 966 5241 Email: jbear@email.unc.edu

Abbreviations: DMSO; Dimethyl Sulfoxide, ECM; extracellular matrix, FAK; Focal Adhesion Kinase, PBS; Phosphate Buffered Saline, MMPs; matrix metalloproteinases

Abstract

Multiple cell types form specialized protein complexes, podosomes or invadopodia and collectively referred to as invadosomes, which are used by the cell to actively degrade the surrounding extracellular matrix. Due to their potential importance in both healthy physiology as well as in pathological conditions such as cancer, the characterization of these structures has been of increasing interest. Following early descriptions of invadopodia, assays were developed which labelled the matrix underneath metastatic cancer cells allowing for the assessment of invadopodia activity in motile cells. However, characterization of invadopodia using these methods has traditionally been done manually with time-consuming and potentially biased quantification methods, limiting the number of experiments and the quantity of data that can be analysed. We have developed a system to automate the segmentation, tracking and quantification of invadopodia in time-lapse fluorescence image sets at both the single invadopodia level and whole cell level. We rigorously tested the ability of the method to detect changes in invadopodia formation and dynamics through the use of well-characterized small molecule inhibitors, with known effects on invadopodia. Our results demonstrate the ability of this analysis method to quantify changes in invadopodia formation from live cell imaging data in a high throughput, automated manner.

Introduction

Migration through a three dimensional environment, such as during embryonic development or metastasis, is a multistage process beginning with the migration of either single cells or groups of cells away from the primary site and into the surrounding ECM. To accomplish this migration, the ECM is commonly degraded, typically through the use of matrix metalloproteinases (MMPs) to form paths through which the cells can move. Invadopodia and podosomes, collectively termed invadosomes, are the two structures most commonly associated with this behavior. In the case of cancer cells and the process of metastasis, the formation of invadopodia that actively degrade the ECM is a common observation (Destaing et al., 2011; Murphy and Courtneidge, 2011). Importantly, while markers such as cortactin and Arp2/3 subunits can help discern these structures from other actin-rich structures, the direct observation of degradation activity is required in order to accurately identify these invasive structures.

Invadopodia were first imaged in Rous sarcoma virus transformed cells using several imaging methodologies including interference reflection and fixed cell labelling (Chen, 1989; Tarone et al., 1985). To measure degradation activity *in vitro*, quantitative imaging assays of invadopodia behaviour have been developed that use fluorescently labeled ECM to visualize regions of degradation caused by invadopodia (Artym et al., 2009). By combining fluorescently labeled ECM and fluorescently labelled intracellular markers of invadopodia, such as cortactin (Artym et al., 2006), cofilin (Stoletov et al., 2013) or actin (Albiges-Rizo et al., 2009), the activity of single invadopodia can be followed through time. The continued development of methods to observe invadopodia formation and ECM degradation has made it possible to quantify the effect of siRNA knockdown or drug treatment on invadopodia dynamics. However, the time-lapse image sets produced using these methods have traditionally been analysed using manual analysis methods which are time-consuming and potentially biased in the selection of which invadopodia will be measured.

In order to improve the reliability of invadopodia measurement systems, we have developed a system to automate the segmentation, tracking and quantification of invadopodia in time-lapse fluorescence image sets at both the single invadopodia level and whole cell level. These methods use the fluorescently labeled ECM images to determine when and where individual invadopodia

96 or cells are degrading the matrix, making detailed studies of invadopodia formation, timing and
97 activity possible. Since these methods were initially developed using LifeAct-GFP as marker of
98 invadopodia, the system does not assume that all bright puncta will become invadopodia and
99 degrade the ECM and instead uses the changes in the underlying ECM to classify puncta. We
100 have made these tools available as open source packages and made a web-based version of the
101 single invadopodia analysis available.

102

103

104

105 **Results**

106 **Identification and Tracking of LifeAct-GFP Puncta**

107 The development of software and subsequent analysis of invadopodia was performed in multiple
108 steps. The first step of analysis involved the development of methods to segment and track single
109 actin aggregates, termed puncta, from images of LifeAct-GFP. After identifying actin puncta, a
110 set of measurements were made from the fluorescent ECM images at each time point to classify
111 the effect of the puncta on the underlying ECM. As only a portion of the population of LifeAct-
112 GFP puncta degrade the matrix, puncta that degrade the matrix are classified as invadopodia.
113 Additional collected properties such as degradation rates were then used in further analyses as
114 described below.

115

116 To identify LifeAct-GFP labelled puncta in WM2664 cells (Figure 1A), untreated and BB94
117 treated cells were imaged by time-lapse microscopy. In order to ensure that the automated
118 system would have decision thresholds similar to that of experts doing a manual analysis, prior to
119 automated analysis, images were manually segmented to identify LifeAct-positive puncta by
120 three independent observers. A consensus of segmentation was reached by majority vote from
121 the manual segmentation, which was then used to test potential segmentation strategies and
122 determine appropriate filters.

123

124 The first stage of the automated segmentation pipeline used a high-pass filter to remove the
125 background noise from the LifeAct-GFP signal (Figure 1B) and then determined the mean and
126 standard deviation of the high-pass filtered pixel intensities for use as thresholds (Haier et al.,

127   2003). To identify individual puncta, a seed-based region-growing segmentation method was

128   used. To identify seed pixels in each image, intensity thresholds from 1-10 standard deviations

129   were tested and these automatically segmented regions were compared to those identified

130   through manual segmentation (Figure 1C). The false positive and negative rates were computed

131   as previously described (Matov et al., 2010). As the seed threshold increased, the rate of false

132   positives decreased, while the rate of false negatives increased. We also tested minimum seed

133   sizes, ranging from 2-10 pixels, and observed the same general behaviour in the false positive

134   and false negative rates as seed size increased. To balance these factors, we empirically selected

135   a standard deviation threshold of 3 and a minimum size of 6 pixels to identify the puncta seeds

136   (Figure 1D).

137

138   After identification of the puncta seeds, a second threshold was selected to expand around each

139   of the identified seed regions. To assess the performance of the seed expansion procedure, we

140   measured the degree of overlap between the manually segmented puncta and the matching

141   computer segmented puncta. We tested thresholds from 0-3 standard deviations from the mean

142   (Figure 1E). As expected, as the seed expansion threshold increases, the false positive rate

143   decreases, while the false negative rate increases. We selected a seed expansion threshold of 1.75

144   to balance these two factors. As a final filter, we also considered the area and ratio between the

145   major and minor axes of the segmented puncta. To determine these filters, we measured these

146   properties in the manually identified puncta (Figure 1F). We used the minimum and maximum

147   values for the area and the major over minus axes ratio as filters for any objects identified after

148   seed identification and expansion. The cell edge was also identified in the LifeAct-GFP signal

149   using a previously published method (Hoshino et al., 2013). The properties for each identified

150   puncta (Figure 1G) were then collected, which included area and the distance of the puncta from

151   the nearest cell edge.

152

153   Each puncta was also tracked through the experiment, using overlap in adjacent frames to

154   connect the segmented puncta. The majority of the identified puncta were present for only one

155   frame (Figure 2A), but a population of puncta that could be followed for 12 frames or more

156   (Figure 2A inset) was also observed. For puncta that live for 12 frames or more, the average area

157 (Figure 2B) and the average distance from the nearest cell edge (Figure 2C) were calculated over

158 time.

159

160 **Determination of ECM Degradation by Puncta**

161 As described previously, degradation of the matrix is a necessary condition for an individual

162 puncta to be classified as a functional invadopodia. This degradation is visible as dark regions

163 that develop in a fluorescently labelled gelatin matrix underneath puncta over time. In order to

164 detect this change in the ECM, the average ECM intensity immediately underneath each puncta

165 and the area in a five pixel border surrounding the puncta was tracked over time (Figure 3A).

166 Areas within the surrounding border occupied by another identified puncta were excluded from

167 quantitation. The difference between the average intensity in the surrounding ECM and the ECM

168 underneath each puncta was used to calculate the local fluorescence difference, so that puncta

169 that have degraded the ECM will have positive values in the local fluorescence difference, while

170 non-degrading puncta will have values near zero. To account for irregularities in the gelatin

171 matrix, the intensity of the matrix before the puncta appeared in the time-lapse image set was

172 also determined. This pre-birth local fluorescence difference was calculated over the same pixels

173 using the image immediately before the appearance of puncta. In cases where the puncta is

174 present at the beginning of the time-lapse, the first image of the ECM time-lapse was used. The

175 pre-birth local difference calculated at each image was used to correct the observed local

176 intensity difference, giving the corrected local intensity difference.

177

178 To classify the puncta as active invadopodia, the values of the local difference, pre-birth local

179 difference and the corrected local difference were analysed. To ensure that sufficient data from

180 each puncta was assessed, we limited our search to only those puncta present in the time-lapses

181 for at least one hour (12 images under our experimental protocol). Application of this filtering

182 constraint left 2,323 untreated puncta and 979 DMSO, 294 BB94, 533 Focal Adhesion Kinase

183 (FAK) inhibitor, 83 PP2 and 125 Purvalanol A treated puncta. For invadopodia, we would expect

184 the local difference and corrected local difference values to be positive (puncta that do not

185 degrade the matrix; see a sample invadopodia in Figure 3B) and for both of these values to

186 average around zero or negative for non-invadopodia puncta (see a sample non-invadopodia

187 puncta in Figure 3C). Next, we tested whether the mean local intensity difference and the mean

188 corrected local intensity difference were statistically different from zero using a t-test. After

189 applying a bonferroni correction for the number of tests run, 336 untreated, 44 control, 12 BB94

190 treated and 35 FAK inhibitor treated puncta were classified as invadpodia. As expected, no

191 actively degrading invadopodia were detected in the PP2 or Purvalanol A treated cells. The mean

192 local corrected difference was greater in the untreated, control and FAK inhibitor treated cells as

193 compared to the BB94 treated cells (Figure 3D). The calculated differences in invadopodia

194 number following drug treatment correlate with previously identified outcomes on invadopodia

195 for each inhibitor tested (Chan et al., 2009; Hoshino et al., 2012; Wang et al., 1994) and

196 demonstrate the accuracy of the automated detection methods developed here. The 7

197 invadopodia identified in BB94 treated cells were manually identified as false positives and we

198 excluded them from further analysis. The low number of false positives identified in the BB94

199 treated cells further demonstrates the improved performance capable through the use of these

200 automated imaging methods.

201

202 **Measurement of Invadopodia Properties**

203 Invadopodia identified in the untreated, control and FAK treated invadopodia were used to

204 measure the mean area of each invadopodia and average distance of invadopodia to the nearest

205 cell edge (Figure 4A, B). No differences were detected in the average area of invadopodia

206 between conditions (Figure 4A). The average distance of invadopodia from the edge of the cell

207 was decreased by 28% in control cells compared to untreated cells and by 38% after treatment

208 with FAK inhibitor (Figure 4B). There was no difference observed in invadopodia distance from

209 the edge between control cells and FAK inhibitor treated cells (Figure 4B). The lifetime of

210 invadopodia showed increases of 45% as compared to the untreated cells following treatment

211 with the FAK inhibitor (Figure 4C).

212

213 The amount of time from puncta formation until maximum degradation was also quantified. To

214 measure this property a smoothed curve was fit to the degradation curve of each invadopodia

215 (e.g. the curve shown in Figure 3B). The earliest time point at which the smoothed values hit

216 90% of the maximum was chosen as the time to maximum degradation. The time to reach

217 maximum degradation was increased by 77% in the FAK treated cells when compared with the

218 untreated cells (Figure 4D).

219

Quantification of Whole-Cell Degradation Behaviors

220

221 To complement the single invadopodia analysis, a system for quantifying the ECM degradation

222 capacity of entire cell populations was also developed. As with the individual invadopodia work,

223 WM2664 cells expressing LifeAct-GFP and exposed to the same drug treatments used for single

224 cell analysis were used to test the capabilities of this system. After image pre-processing, cells in

225 the LifeAct-GFP images (Figure 5A) were identified using the same algorithm as that used to

226 find the cell outline in the single invadopodia analysis (Figure 5B). To minimize the number of

227 cell clusters found and make sure results describe measurements for individual cells, we

228 quantified the areas of all observed single cells and multi-cell clusters (Figure 5C). We

229 empirically set a minimum size threshold of 1,500 pixels (107 μm^2) to exclude small debris and a

230 maximum size threshold of 20,000 pixels (1422 μm^2) to exclude cell clusters from further

231 analysis.

232

233 By identifying and tracking individual cells through time, we observed a bimodal distribution of

234 cell lifetimes (Figure 5D). Objects present for less than 10 hours were often non-adhered cell

235 bodies or other debris in the field of view and were excluded from further analysis. In parallel

236 with the cell images, images were also taken of the fluorescent ECM (Figure 5E). Using the

237 segmented cells and the intensity of the underlying matrix, we were able to observe both cells

238 that degraded the matrix as well as those that did not (Figure 5F).

239

Determination of Cellular ECM Degradation

240

241 The segmented cell and ECM images (Figure 5) were used to classify cells as either degraders or

242 non-degraders. To accomplish this, methods similar to the analysis of single invadopodia were

243 used (Figure 6A). More specifically, for cells identified in each image, the average ECM

244 intensity underneath and within a 40 pixel border around each cell was measured, while

245 excluding any region overlapping with another cell and the corresponding regions in the prior

246 ECM image. The average change in fluorescence intensity from the prior image to current image

247 and in the surrounding 40 pixel border was then calculated. To allow these values to be

248 compared across differing ECM intensity regions, the values were saved as the percentage

249 difference between the ECM intensity underneath each cell and the surrounding region.

250 Therefore, invading cells (i.e. those degrading the matrix) would be expected to have lower ECM

251 intensities immediately underneath the cell. We then collected time-series images for each cell

252 present for at least ten hours (example time-series is shown in Figure 6B).

253

254 In addition to the image-by-image assessment of the percentage of the ECM degraded, the

255 overall percentage of fluorescent ECM degraded by each cell was also assessed (Figure 6C). To

256 find the overall degradation percentage for each cell, the area of influence for each cell was

257 determined by finding the amount of time the cell covered each pixel location in the field of

258 view. Any pixel location covered for at least 2.5 hrs was considered to be in that cell's area of

259 influence. The change in fluorescence intensity from the first image of the ECM time-lapse and

260 the area surrounding the cell was then calculated in the same manner as when calculating the

261 percentage change from image to image.

262

263 Each cell was classified as degrading or non-degrading on a per image basis using the between

264 images and total ECM degradation percentages calculated. As the BB94-treatment is expected to

265 block all activity of the MMPs, degradation percentages found in the BB94 treated cells were

266 used as a negative control. We empirically assessed the potential cut-off values to minimize the

267 number of false positives (ie: the number of BB94-treated cells classified as degraders).

268

269 **Measurement of Matrix Degrading Behaviors**

270 With each cell classified as a degrader or non-degrader, we calculated the percentage of cells in

271 each class at half hour intervals throughout the experiment (Figure 7A). In general, treatment

272 with the FAK inhibitor tended to increase the percentage of degrading cells, while Purvalanol A

273 decreased the percentage of degrading cells. Only eight degrading cells were detected under

274 BB94 treatment and these were manually conformed as false positives and excluded from further

275 analysis. These results are comparable to those observed at the single invadopodia level and

276 again confirm the accuracy and low rate of false positives obtained using the developed

277 automated analysis methods.

278

279 The area of ECM degraded by each cell was also quantified. To find the degraded regions of the

280 matrix, the first and last images of the time-lapse were compared; any region where the intensity

281 had decreased by 20% was marked as degraded. These degraded areas were assigned to each cell
282 according to the previously defined area of influence (Figure 7B). FAK inhibitor significantly
283 increased the area degraded by each cell (62% increase compared to control), while PP2 and
284 Purvalanol A each decreased the average area degraded (61% decrease compared to control).
285 Similarly, the rate of degradation was also quantified by dividing the total area degraded by the
286 cell lifetime (Figure 7C). For this property we observed similar trends to the total area degraded
287 with FAK inhibitor treated cells having a higher rate of degradation (23% increase compared to
288 control), while in the PP2-treated cells and Purvalanol A-treated cells, there was a decrease in the
289 degradation rate (37% and 43% decreases compared to control).

290
291
292

293 **Discussion**

294 Understanding the process of metastasis is an as yet unresolved issue in cancer biology and
295 whose study has important ramifications in disease management and therapy. As the escape and
296 migration of cancer cells from the primary tumor is preceded by degradation of the ECM,
297 invadopodia may play a highly significant role. However, the quantification of their dynamic
298 behaviours has been relatively limited. The framework presented here provides a reliable
299 approach for the quantitative analysis of invadopodia behavior in both single cells and in cell
300 populations over time. To develop this system, we gathered time-lapse image sets of the
301 WM2664 metastatic cancer cell line expressing LifeAct-GFP (Riedl et al., 2008) forming
302 invadopodia over an Alexa 568-labeled ECM. Since F-actin, as labeled by LifeAct, is not a
303 conclusive marker of invadopodia on its own, we used the images from the labeled ECM to
304 classify each F-actin puncta as either an invadopodia or not based on changes in the ECM
305 intensity over time. After classification of the puncta, our system calculates several dynamic
306 invadopodia properties such as lifetime and the time taken to reach maximum degradation levels.
307 To complement the analysis conducted at the single invadopodia level, we also designed an
308 automated system that follows and quantifies degradation activity at the whole cell level. This
309 approach uses images taken at a lower magnification (20X in our experiments) to gather a
310 representative picture of the degradation behaviour of cellular populations through time. Using
311 this system, we can begin to explore dynamic aspects of cancer cell heterogeneity at the single

312   cell level. For instance, the percentage of cells that have degraded the matrix as well as the rate

313   and total amount of degradation performed by each cell can be quantified. Both of these systems

314   were tested using a set of small molecule inhibitors previously demonstrated to block or enhance

315   invadopodia formation (Chan et al., 2009; Hoshino et al., 2012; Wang et al., 1994). Our results

316   are supported by earlier findings but also significantly extend the amount and degree to which

317   invadopodia and cell degradation behaviors can be quantified, all within an automated image

318   analysis framework.

319

320   Many different pharmaceuticals and their potential effects on invadopodia have been examined

321   in fixed or live cell assays in the past. These include drug treatments such as BB94, Purvalanol

322   A, and PP2 which are hypothesized to inhibit the formation of invadopodia (Chan et al., 2009;

323   Hoshino et al., 2012; Wang et al., 1994). BB94 inhibits MMPs, which are the enzymatic

324   components of invadopodia that degrade the matrix (Wang et al., 1994). The effect of BB94

325   treatment is that formed puncta do not go on to degrade the matrix and are thus not formally

326   classified as invadopodia (observation of degradation is a necessary requirement for

327   classification of puncta as invadopodia) (Linder et al., 2011). Live cell imaging experiments of

328   cancer cells treated with BB94 act as means to set thresholds to minimize the number of false

329   positives detected by the system. Purvalanol A inhibits cyclin-dependent kinase which in turn

330   inhibits the tyrosine kinase Src, and PP2 is a more direct inhibitor of the tyrosine kinase Src and

331   other members of the Src family. Src is known to be involved in invadopodia formation that

332   consequently decreases when Src is inhibited by either Purvalanol A or PP2 (Chan et al., 2009;

333   Hoshino et al., 2012). On the other hand FAK Inhibitor II is hypothesized to enhance the

334   formation of invadopodia. Studies using FAK knockdown have demonstrated an increase in

335   invadopodia suggesting FAK regulates and suppresses invadopodia formation (Chan et al.,

336   2009). Therefore FAK inhibitor II, which decreases FAK autophosphorylation and activation,

337   should enhance invadopodia formation. Automated analysis as presented in the current study has

338   shown the same decrease in invadopodia formation using BB94, PP2 and Purvalanol A, as well

339   as an increase in invadopodia formation following treatment with FAK inhibitor II. Our results

340   clearly demonstrate that the software developed accurately detects known changes in

341   invadopodia formation in response to characterized perturbations.

342

343 A wide range of other fluorescent probes and tools are also capable of being used in the
344 automated analyses described here, such as Tks5 (Tang et al., 2013) or cortactin (Artym et al.,
345 2006). Invadopodia proteins need to be fluorescently tagged and be present at invadopodia
346 during the degradation process in order to be assessed using our system. Many of these
347 alternative tags should, in fact, more reliably mark invadopodia than the LifeAct F-actin label
348 used in this work, making analysis with these markers less likely to result in false positives and
349 decrease the requirement for manual confirmation of potential false positives as required in the
350 BB94 samples in the current study. The cell population analysis system can also be adapted to
351 use alternative cell markers such as dyes or membrane associated fluorescent markers and may
352 be further improved by the addition of a nuclear marker, making it possible to reliably split cell
353 clumps using a watershed segmentation (Malpica et al., 1997). Alternative ECM labeling
354 methodologies such as dye-quenched gelatins, or other ECM substrates such as fibronectin can
355 similarly be utilized. This analysis tool is readily adaptable outside of the field of cancer
356 research, for instance, for the examination of the related invasive structure podosomes, which are
357 found in highly migratory cells such as osteoclests and macrophages (Albiges-Rizo et al., 2009;
358 Block et al., 2008).

359

360 The software to process the labeled puncta in single cells and in cell populations through time
361 has been released as open source packages available through the Gomez lab github repository
362 (https://github.com/gomezlab/). In addition, the single cell analysis of individual puncta can be
363 performed through a web application (http://ias.bme.unc.edu/), which does not require the user to
364 download or install any software to process a set of invadopodia images. These two
365 complementary analysis systems allow the quantification of invadopodia behavior at the single
366 invadopodia and single cell levels. Combined with high throughput imaging methodologies, this
367 analysis tool will be highly useful in screening small molecule inhibitors for efficacy in
368 inhibiting invadopodia formation in cancer cells as well as quantifying genetic and cellular
369 heterogeneity that may underlie related metastatic behaviors.

370
371
372
373

Materials and Methods

Reagents

All chemicals and reagents were purchased from Sigma (St Louis, MO) unless otherwise stated. The BB94, Purvalanol A, FAK Inhibitor II and PP2 compounds were all purchased from EMD BioSciences (La Jolla, CA). All drugs were soluble in DMSO, which was used as a control for all experiments. The BB94 and FAK Inhibitor II were used at a final concentration of 5 μM, while Purvalanol A was used at 2 μM and PP2 was used at 10 μM. The Alexa Fluor 568 protein labeling kit used to label the gelatin matrix was purchased from Invitrogen (Eugene, OR), as were all cell culture reagents. Fugene 6 used for transfections was purchased from Roche Diagnostics (Indianapolis, IN). For dynamic visualization of actin, the LifeAct peptide (Riedl et al., 2008) was cloned into the previously described pLL 5.0 GFP Lenti-viral base vector (Wang and McNiven, 2012).

Cell Lines and Culture

Wild Type and LifeAct-GFP WM2664 cell lines and 293FT Hek cells were maintained in DMEM with 10% FBS and 1% PSG at 37°C in a humidified atmosphere with 5% CO_2. Lentiviral production was performed as previously described in (Wang and McNiven, 2012). Briefly, lentiviral expression plasmids were transfected into 293FT cells with the construct of interest using Fugene6. After 24 hrs, media is changed and viral media is applied to 30-50% confluent WM2664 cells in a 6-well dish for 48hrs. Fluorescent cells were FACS sorted for the 20-80% range of GFP positive cells.

Fluorescent Gelatin Matrix

To prepare ECM substrate for the invadopodia assays, 0.2% Type A gelatin from porcine skin was fluorescently labeled using the Alexa Fluor 568 protein labeling kit according to the manufacturer instructions. Culture vessels were coated at room temperature with thin layers of 20% poly-L-lysine for 20 mins followed by 0.5% glutaraldehyde (Electron Microscopy Sciences, Hatfield, PA) for 15 mins. An 8:1 ratio of unlabeled to labeled gelatin was prepared and incubated on culture vessels for 10 mins. Following gelatin incubation a 5 mg/mL solution of $NaBH_4$ (Fisher Scientific, Fair Lawn, NJ) was incubated for 15 mins to quench any remaining

404   glutaraldehyde. Between each level of coating, the dishes were washed three times with

405   phosphate buffered saline (PBS).

406

407   *Single Cell Assay Imaging Parameters*

408   LifeAct-GFP WM2664 cells were plated (+/- inhibitors) onto heated bioptech dishes (Bioptech

409   Inc., Butler, PA) coated with Alexa Fluor 568 labeled gelatin, as described above. Cells were

410   allowed to equilibrate on the microscope 1 hr before imaging. Random fields of view were

411   selected and time-lapse microscopy was performed on an Olympus IX- 81 inverted microscope

412   (60x, 1.3NA objective) with a Hamamatsu CCD camera (model c4742-80-12AG) and a Prior

413   Lumen200Pro epifluorescence system (Olympus America, Center Valley, PA) on a heated stage

414   with heated lid receiving a constant stream of humidified 5% CO_2 to maintain cell viability.

415   Images were captured in both the 488 and 568 channels every 5 mins for 12 hrs using

416   MetaMorph Imaging software (Molecular Devices, Sunnyvale, CA).

417

418   *Cell Population Assay Imaging Parameters*

419   LifeAct-GFP WM2664 cells (+/- inhibitors) were plated onto MatTek 35 mm glass bottom

420   dishes (MatTek Corporation, Ashland, MA) coated with Alexa Flour 568 labeled gelatin, as

421   described above. Cells were allowed to equilibrate in the incubation chamber of the microscope,

422   heated to 37°C with a humidified atmosphere of 5% CO_2, for 1 hr before imaging. Cells were

423   imaged in the Olympus VivaView microscope with a 20x/0.75NA objective and morotized

424   magnification changer set to 1x, using a Hamamatsu Orca R2 cooled CCD camera (Olympus

425   America, Center Valley, PA). A template was used to select 25 predetermined positions in each

426   dish and images in the 488 and 568 channels were captured every 30 mins for 25 hrs.

427

428   *Invadopodia Analysis*

429   Before analyzing, the fluorescent ECM images were photobleach corrected. To ensure that the

430   degradation of ECM was not incorrectly identified as photobleaching, only pixels outside the cell

431   bodies were considered when photobleaching correction was applied. Images were then flat-field

432   corrected and the single cell time-lapse images for single cell assays were registered (the cell

433   population movies did not require registration). In the ECM images used for the single

434   invadopodia analysis, the average fluorescence outside the cell bodies was set to 1000 to allow

435 the local difference values to be compared between ECM preparations. The LifeAct-GFP images
436 for the single invadopodia analysis were not pre-processed. The LifeAct-GFP images for the
437 population analysis were flat-field corrected. The analysis software uses a high-pass filter and
438 threshold to identify regions of high actin concentration (potential invadopodia) that co-localize
439 with underlying ECM degradation to identify active invadopodia and track them through time.

440
441
442

Acknowledgements

465

References

Albiges-Rizo, C., O. Destaing, B. Fourcade, E. Planus, and M.R. Block. 2009. Actin machinery and mechanosensitivity in invadopodia, podosomes and focal adhesions. *Journal of cell science*. 122:3037-3049.

Artym, V.V., K.M. Yamada, and S.C. Mueller. 2009. ECM degradation assays for analyzing local cell invasion. *Methods Mol Biol*. 522:211-219.

Artym, V.V., Y. Zhang, F. Seillier-Moiseiwitsch, K.M. Yamada, and S.C. Mueller. 2006. Dynamic interactions of cortactin and membrane type 1 matrix metalloproteinase at invadopodia: defining the stages of invadopodia formation and function. *Cancer research*. 66:3034-3043.

Block, M.R., C. Badowski, A. Millon-Fremillon, D. Bouvard, A.P. Bouin, E. Faurobert, D. Gerber-Scokaert, E. Planus, and C. Albiges-Rizo. 2008. Podosome-type adhesions and focal adhesions, so alike yet so different. *Eur J Cell Biol*. 87:491-506.

Chan, K.T., C.L. Cortesio, and A. Huttenlocher. 2009. FAK alters invadopodia and focal adhesion composition and dynamics to regulate breast cancer invasion. *The Journal of cell biology*. 185:357-370.

Chen, W.T. 1989. Proteolytic activity of specialized surface protrusions formed at rosette contact sites of transformed cells. *J Exp Zool*. 251:167-185.

Destaing, O., M.R. Block, E. Planus, and C. Albiges-Rizo. 2011. Invadosome regulation by adhesion signaling. *Curr Opin Cell Biol*. 23:597-606.

Haier, J., T. Korb, B. Hotz, H.U. Spiegel, and N. Senninger. 2003. An intravital model to monitor steps of metastatic tumor cell adhesion within the hepatic microcirculation. *Journal of gastrointestinal surgery : official journal of the Society for Surgery of the Alimentary Tract*. 7:507-514; discussion 514-505.

Hoshino, D., K.M. Branch, and A.M. Weaver. 2013. Signaling inputs to invadopodia and podosomes. *Journal of cell science*. 126:2979-2989.

Hoshino, D., J. Jourquin, S.W. Emmons, T. Miller, M. Goldgof, K. Costello, D.R. Tyson, B. Brown, Y. Lu, N.K. Prasad, B. Zhang, G.B. Mills, W.G. Yarbrough, V. Quaranta, M. Seiki, and A.M. Weaver. 2012. Network analysis of the focal adhesion to invadopodia transition identifies a PI3K-PKCalpha invasive signaling axis. *Science signaling*. 5:ra66.

Linder, S., C. Wiesner, and M. Himmel. 2011. Degrading devices: invadosomes in proteolytic cell invasion. *Annu Rev Cell Dev Biol*. 27:185-211.

Malpica, N., C.O. de Solorzano, J.J. Vaquero, A. Santos, I. Vallcorba, J.M. Garcia-Sagredo, and F. del Pozo. 1997. Applying watershed algorithms to the segmentation of clustered nuclei. *Cytometry*. 28:289-297.

Matov, A., K. Applegate, P. Kumar, C. Thoma, W. Krek, G. Danuser, and T. Wittmann. 2010. Analysis of microtubule dynamic instability using a plus-end growth marker. *Nat Methods*. 7:761-768.

504 Murphy, D.A., and S.A. Courtneidge. 2011. The 'ins' and 'outs' of podosomes and invadopodia:
505   characteristics, formation and function. *Nat Rev Mol Cell Biol*. 12:413-426.

506 Riedl, J., A.H. Crevenna, K. Kessenbrock, J.H. Yu, D. Neukirchen, M. Bista, F. Bradke, D.
507   Jenne, T.A. Holak, Z. Werb, M. Sixt, and R. Wedlich-Soldner. 2008. Lifeact: a versatile
508   marker to visualize F-actin. *Nat Methods*. 5:605-607.

509 Stoletov, K., J. Strnadel, E. Zardouzian, M. Momiyama, F.D. Park, J.A. Kelber, D.P. Pizzo, R.
510   Hoffman, S.R. VandenBerg, and R.L. Klemke. 2013. Role of connexins in metastatic
511   breast cancer and melanoma brain colonization. *Journal of cell science*. 126:904-913.

512 Tang, H., A. Li, J. Bi, D.M. Veltman, T. Zech, H.J. Spence, X. Yu, P. Timpson, R.H. Insall,
513   M.C. Frame, and L.M. Machesky. 2013. Loss of Scar/WAVE complex promotes N-
514   WASP- and FAK-dependent invasion. *Current biology : CB*. 23:107-117.

515 Tarone, G., D. Cirillo, F.G. Giancotti, P.M. Comoglio, and P.C. Marchisio. 1985. Rous sarcoma
516   virus-transformed fibroblasts adhere primarily at discrete protrusions of the ventral
517   membrane called podosomes. *Exp Cell Res*. 159:141-157.

518 Wang, X., X. Fu, P.D. Brown, M.J. Crimmin, and R.M. Hoffman. 1994. Matrix
519   metalloproteinase inhibitor BB-94 (batimastat) inhibits human colon tumor growth and
520   spread in a patient-like orthotopic model in nude mice. *Cancer Res*. 54:4726-4728.

521 Wang, Y., and M.A. McNiven. 2012. Invasive matrix degradation at focal adhesions occurs via
522   protease recruitment by a FAK-p130Cas complex. *The Journal of cell biology*. 196:375-
523   385.

524 Yamaguchi, H., M. Lorenz, S. Kempiak, C. Sarmiento, S. Coniglio, M. Symons, J. Segall, R.
525   Eddy, H. Miki, T. Takenawa, and J. Condeelis. 2005. Molecular mechanisms of
526   invadopodium formation: the role of the N-WASP-Arp2/3 complex pathway and cofilin.
527   *The Journal of cell biology*. 168:441-452.

528
529
530
531
532
533
534
535
536
537
538
539
540

Figure Legends

Figure 1. Segmentation of Puncta from LifeAct-GFP images.

(A) Epifluorescence image of WM2664 cell expressing LifeAct-GFP. (B) Image from Part A passed through a high-pass filter. (C) Contour plots showing the detection errors for identification of puncta seeds. (D) Locations of puncta seeds accepted with minimum seed size 6 and high-passed threshold of 3. (E) Error rates on a pixel basis as a function of the puncta expansion threshold. (F) Puncta area plotted versus ratio between major and minor axes in puncta manually identified in either control or BB94 treated cells. (G) Locations of segmented LifeAct-GFP puncta based on seeding, expansion, area and major over minor axes filtering.

Figure 2. Properties of Segmented and Tracked Puncta in Control Cells

(A) Histogram of the lifetime of the segmented puncta. Inset graph shows the lifetime of puncta with lifetime of 12 frames or more. (B) Histogram of the average puncta area for puncta with lifetimes over 1 hr. (C) Histogram of the distance to the nearest cell edge.

Figure 3. Measurement of ECM degradation underneath single puncta.

(A) Cartoon representation of a single puncta and the corresponding ECM underneath that degrading puncta. (B) Small multiple visualization of a single degrading puncta from a control cell and corresponding ECM intensities. The puncta is outlined in green, while the region classified as the local background is shaded purple. The first column shows the LifeAct and ECM images immediately before puncta formation and the last column shows the same areas immediately after puncta disappearance. (C) Small multiple visualization of a non-degrading puncta. (D) Boxplots of the mean local corrected difference in four of the experimental conditions. The box indicates the 25th and 75th percentiles, while the bold line indicates the median and the whiskers extend to 1.5 times the interquartile range. * indicates $p<0.05$ by t-test.

571   **Figure 4**. Properties automatically extracted from the identified invadopodia. (A) The average

572   area of invadopodia. (B) The average distance from the cell edge of invadopodia. (C) The

573   lifetime of invadopodia. (D) The average time to maximum matrix degradation.

574

575

576   **Figure 5**. Identification of LifeAct-GFP Expressing WM2664 Cells. (A) Sample LifeAct-GFP

577   image from a 25 hr time-lapse experiment after photobleaching and flat-field correction. (B)

578   Same image as in part A, with the segmented cells outlined in yellow. (C) The distribution of

579   object sizes detected based on intensity thresholding. (D) The distribution of the lifetime of

580   objects detected in the control time-lapse image sets. (E) Sample fluorescent ECM image from

581   the same time and field as in part A. (F) The ECM channel in the same field as in part E, at the

582   end of the 25 hr experiment. The two sub-images show the first and last image of two cells

583   outlined in red identified in the field. The lower portion of each sub-image shows the ECM

584   channel immediately underneath each cell.

585

586

587   **Figure 6**. Determination of Single Cell Degrader Status. (A) Cartoon representation of two cells

588   of which one cell degrades the matrix (Cell #1) and another non-degrading cell (Cell #2). Also

589   shown are the overlapping areas of the cell location and the results of comparing the first and last

590   images from the image set. (B) Example small multiple tracks of single cells through time and

591   the corresponding measurment of the percent of matrix degraded between each image. The

592   colors outlining each image on the left corresponds to the same color line in the plot on the right

593   (C) Boxplots of the overall percentage of fluorescent ECM removed underneath control, DMSO

594   treated and BB94 treated cell. * indicate $p<0.05$ via t-test.

595

596

597   **Figure 7**. Properties of Degrading Cells (A) Percentage of cells classified as degraders over the

598   25 hrs imaging time frame. Percentages are averages from several experiments (n=5 control, n=2

599   BB94, n=14 DMSO, n=4 PP2, n=3 Purvalanol A and n=4 FAK Inhibitor). (B) The total area and

600   (C) rate of degradation from each cell classified as an invader, * $p<0.05$ via t-test
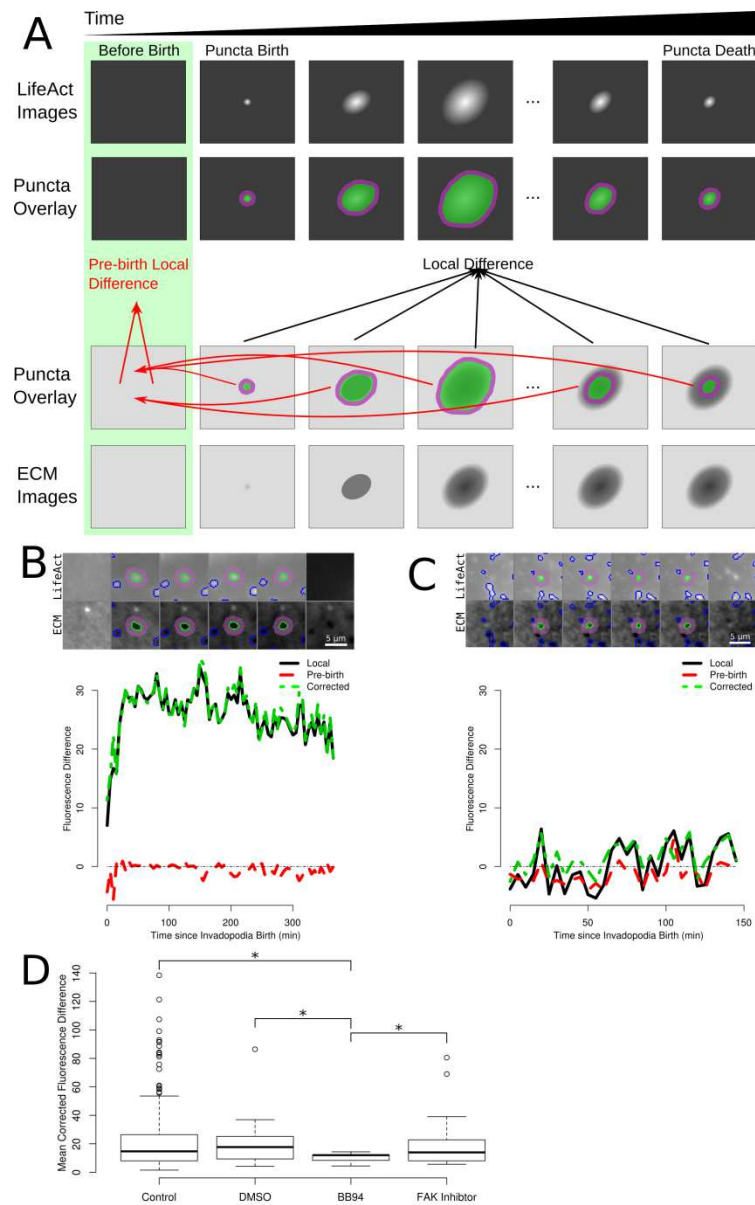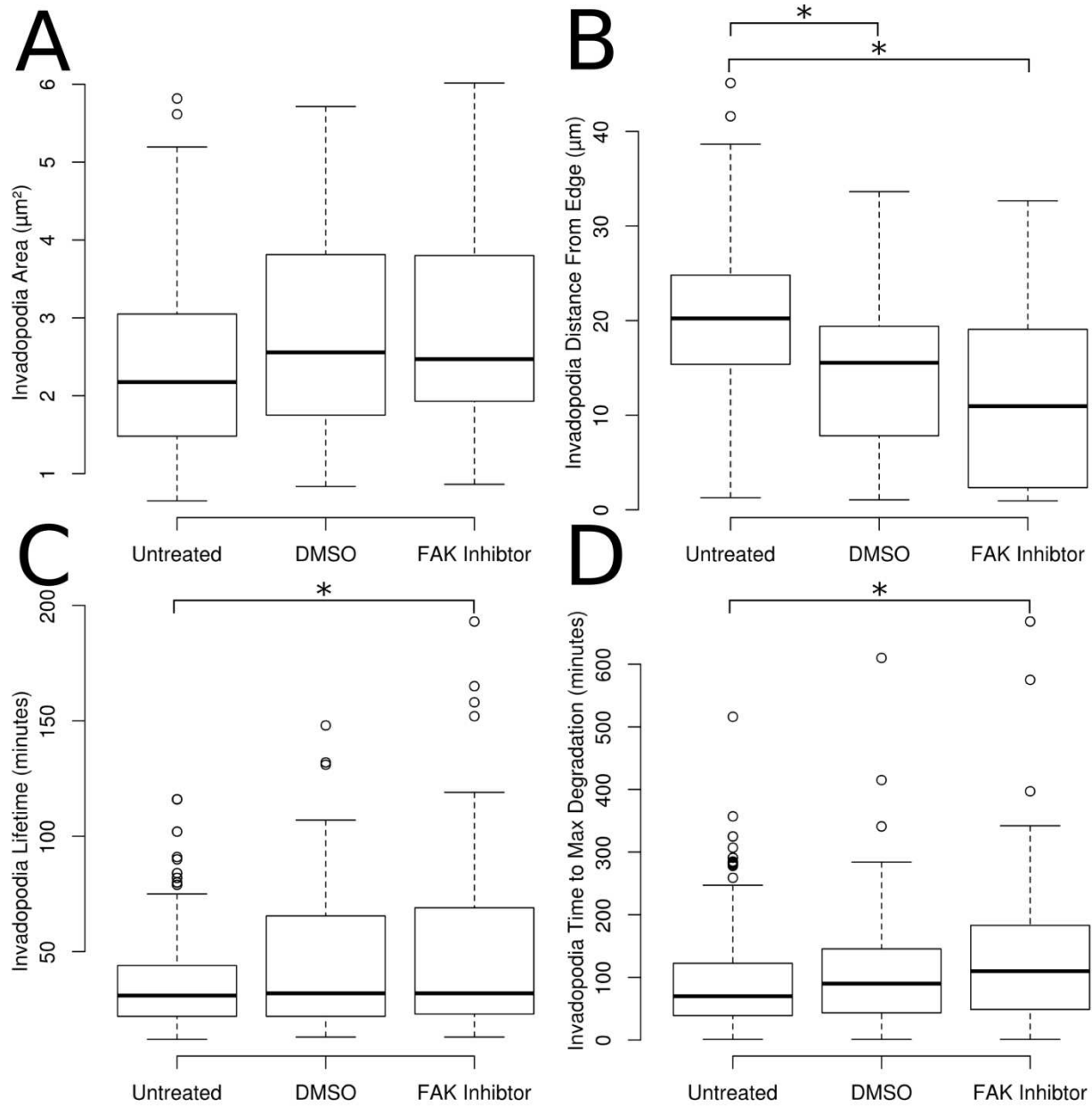
FIGURE 1
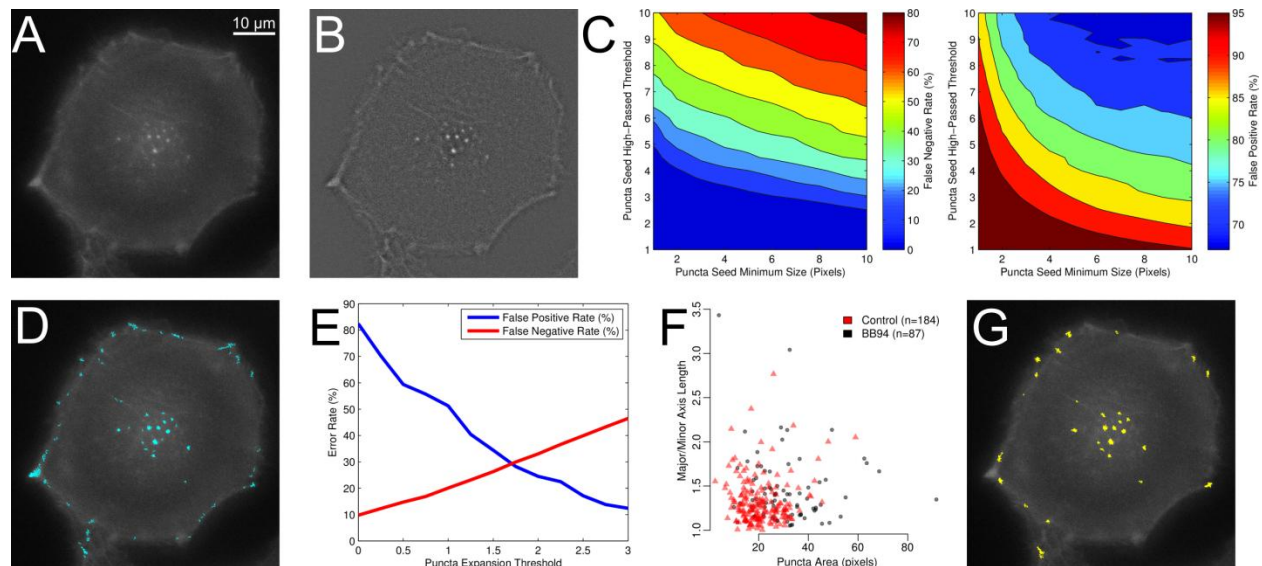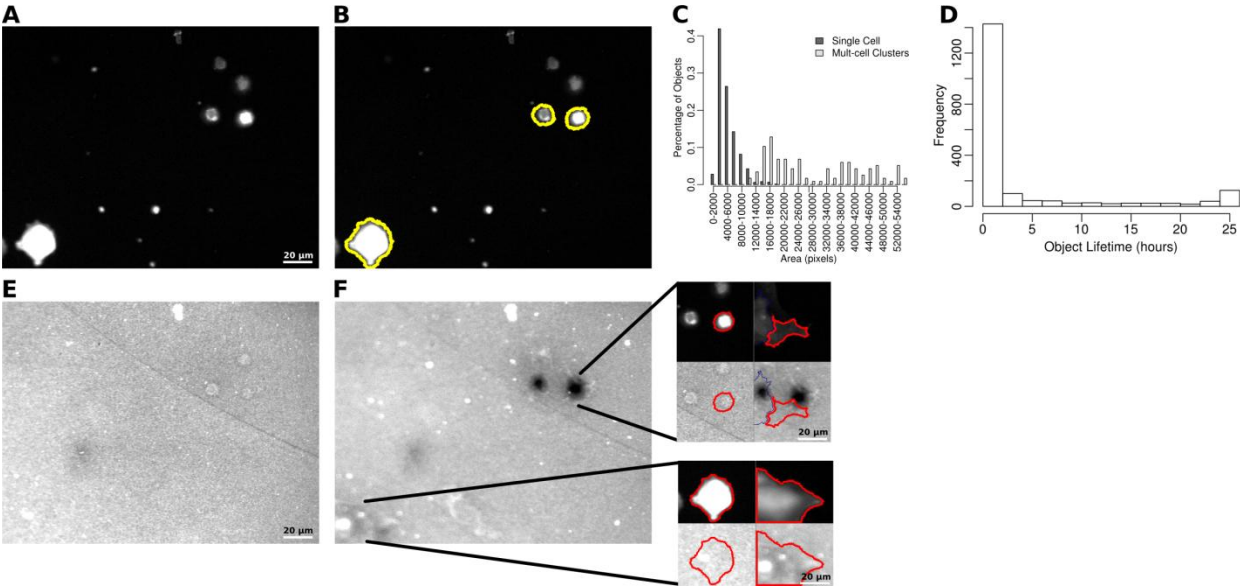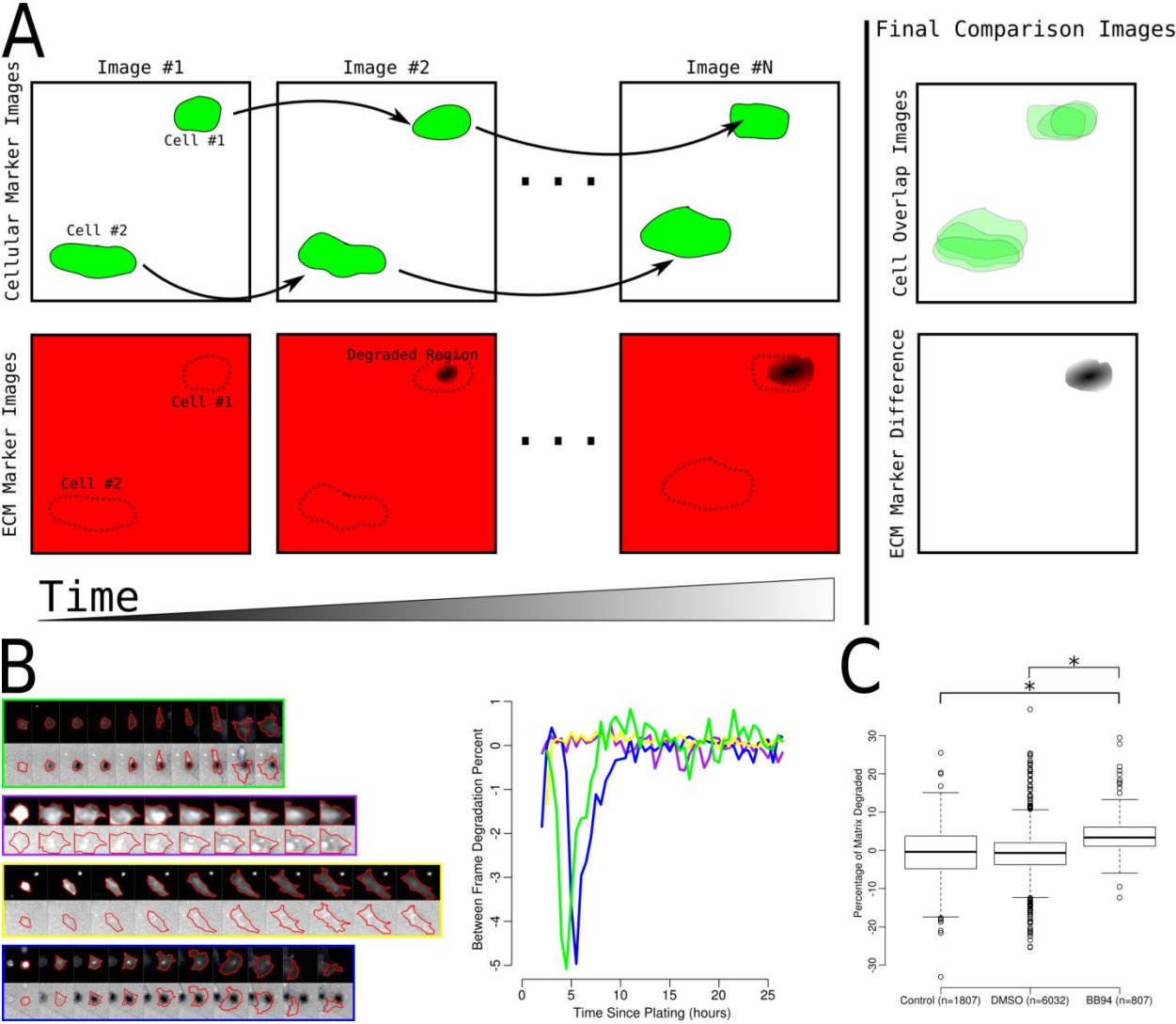
FIGURE 2
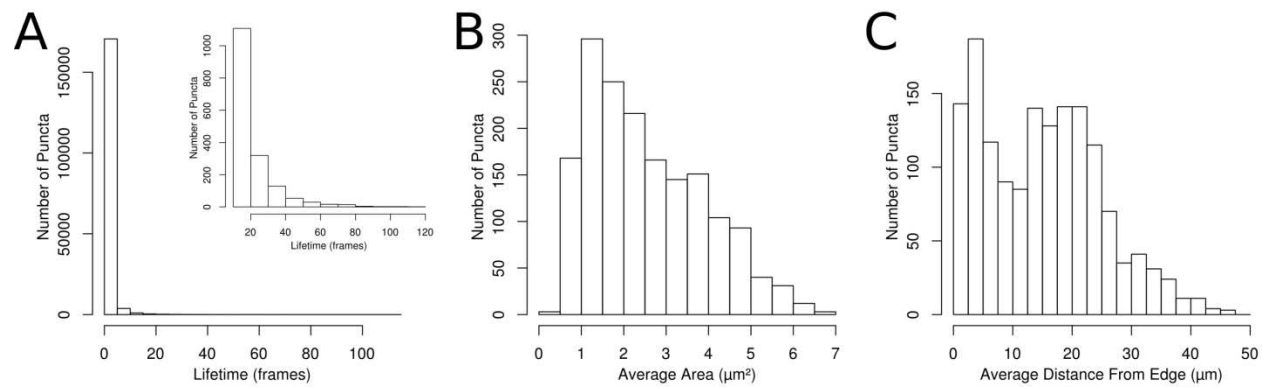
FIGURE 3

FIGURE 4

FIGURE 5

FIGURE 6

FIGURE 7